Theoret. Comput. Fluid Dynamics (1995) 7: 217–240

Theoretical and Computational Fluid Dynamics

Large-Eddy Simulation of Nonlinear Evolution and Breakdown to Turbulence in High-Speed Boundary Layers[1]

Nabil M. El-Hady[2]

Analytical Services and Materials, Inc.,
Hampton, VA 23666, U.S.A.

Thomas A. Zang

NASA Langley Research Center,
Hampton, VA 23681, U.S.A.

Communicated by M.Y. Hussaini

Received 13 July 1993 and accepted 7 June 1994

Abstract. The nonlinear evolution and laminar–turbulent breakdown of a boundary-layer flow along a cylinder at Mach 4.5 is investigated with large-eddy temporal simulation. The results are validated using the direct numerical simulation data of Pruett and Zang. The structure of the flow during the transition process is studied in terms of the vorticity field. The subgrid scales are modeled dynamically, where the model coefficients are determined as part of the solution from the local resolved field. In the numerical simulation the dynamic-model coefficients are obtained by using both the strain-rate contraction of Germano *et al.* and the least-squares contraction of Lilly; they produced some differences in the details of the vorticity structure inside the transition region. A new dynamic model that utilizes the second-order velocity structure function is used to parametrize the small-scale field. The evolution to turbulence is successfully simulated with dynamic subgrid-scale modeling at least in terms of average quantities as well as vorticity fields. This is achieved with one-sixth of the grid resolution used in direct numerical simulation.

1. Introduction

In high-speed boundary-layer flows the physics, prediction, and control of the laminar–turbulent transition process are of increasing fundamental, as well as technological, importtance because of such national projects as the design of the High-Speed Civil Transport (HSCT) and the National Aero-Space Plane (NASP). In contrast to the vast progress that has been made in understanding the different mechanisms of laminar breakdown to turbulence in incompressible flows, progress has been much slower for compressible flows because of the inherent complexity of high-speed numerical and laboratory experiments.

Although the road to transition and laminar breakdown mechanisms are poorly understood in high-speed flows, it is believed that it involves several stages analogous to the incompressible case. First, an initial stage of linear instability of small disturbances, called primary instability, is well

[1] This work was sponsored by the Theoretical Flow Physics Branch of the Fluid Mechanics Division of NASA Langley Research Center under Contract NAS1-19320.

[2] Present address: Advanced Technology, P.O. Box 1007, Yorktown, VA 23693, U.S.A.

described by the compressible stability equations. (See [1].) Multiple eigenvalues of high-frequency, amplified, and damped modes (Mack modes) appear in the solution of these equations. The first of the Mack modes is called the second mode, which is the most unstable of all the modes as a two-dimensional disturbance. The linear stage is followed by a second stage, where apparent nonlinearity is revealed by amplification of three dimensionality and the high growth rate of these disturbances. This is generally accepted as a necessary prerequisite for transition even at high speeds. At this stage the disturbances are still weak and nonlinear distortion to the mean flow can be negligible. Theoretical studies of secondary instability mechanisms in high-speed flows (e.g., [2] and [3]) have indicated that the growth rate of these three-dimensional disturbances is more gradual; it persists for a long distance downstream, unlike the explosive and fast growth that was observed in incompressible flows. This may lead, in high-speed flows, to transition regions that are quite lengthy. Finally, a strong nonlinear stage takes place with high and intense fluctuations that lead to the inevitable fully turbulent regime.

Experimental studies at high speeds have been reviewed by Kendall [4]. These studies stressed the fact that the second mode is the dominant instability in the high-speed range and is responsible for the production of persisting, well-ordered, "rope-like" waves that were optically detected near the boundary-layer edge. However, Stetson and Kimmel [5] have indicated that these "rope-like" waves appear to exhibit a three-dimensional structure which was unresolved due to experimental limitations (using a single hot wire).

Classical linear stability and secondary instability theories are not capable of describing the flow structure in the final stage that leads to laminar breakdown and afterwards. The recent approach of parabolized stability equations (PSE) [6], [7] also has limitations and can describe the flow structure until just after the onset of transition. The flow structure during transition can only be described with direct numerical simulation (DNS). However, the application of compressible DNS to the laminar–turbulent transition process is an exceedingly expensive task because of the wide range of length scales present in the later stages of transition; hence, more resolution is needed in this stage than for laminar or fully turbulent flow. Typical temporal DNS computations require many hundreds of supercomputer hours; typical spatial DNS computations require thousands of hours. Because of its high computational requirement, DNS is usually used to simulate a forced transition to focus on the later stages of the transition process.

With the increased interest in boundary-layer transition of high-speed flows, given the high cost of compressible DNS and the problems associated with high-speed laboratory experiments, other, less computationally intensive, methods are needed for engineering purposes. A large number of ongoing efforts by different researchers are aimed at developing such less computationally intensive methods that will make a distinct technological contribution to expanding the state of the art in this field with large-eddy simulation (LES).

Developing models for the small-subgrid scales remains the central issue in LES. Contrary to turbulent flows, the subgrid-scale (SGS) model used for transitional flows is required to capture several stages: the primary, the secondary (or early nonlinear), and the fully nonlinear stages. The model is also required to predict accurately the transition onset, the transition region, and the fully turbulent stage. A review of transition-region modeling was recently given by Singer [8]. The application of LES to transitional flows dictates numerous modifications and extensions for the conventional SGS models that are used for turbulent flows. Although the Smagorinsky eddy-viscosity SGS model [9] remains the most popular subgrid model in LES for incompressible flows, it suffers from serious limitations: the single constant of the model must be tuned for each type of flow, the model is very dissipative specially in the laminar region, the model behavior near the wall is inadequate, and the model poorly predicts the individual elements of the stress tensor. Several modifications to this model have been made; Moin and Kim [10] used a damping function to account for the near-wall effects and Piomelli and Zang [11] used a scale function to avoid the known excessive damping of the SGS motion. Piomelli *et al.* [12] used a modified Smagorinsky model with both damping and scale functions and applied it to the incompressible flat-plate transitional boundary layer. The results compare quite well with the corresponding DNS calculations.

Other investigators have used the structure-function model in LES, which is another model of the eddy-viscosity type. The structure-function model roots back to the concept of spectral eddy coeffi-

cients of Kraichnan [13], where in a simplified formulation by Chollet and Lesieur [14], the eddy coefficients are a function only of time through the kinetic energy spectrum at the cutoff (i.e., independent of wave number). This ensures that the eddy coefficients remain equal to zero as long as there is no energy at the cutooff, a feature that is necessary for simulation of laminar–turbulent transition. Metais and Lesieur [15] and Comte *et al.* [16] implemented this model in physical space, with the kinetic energy spectrum calculated from the velocity differences using the second-order velocity structure function. In their study of turbulent flow on a backward-facing step, Silveira *et al.* [17] have shown that the eddy viscosity calculated by using the structure-function model gives a better agreement with experimental results than Smagorinsky's formulation.

Recently, Germano [18] and Germano *et al.* [19] have introduced an innovative procedure for dynamic modeling of the SGS for incompressible flows. This procedure uses the information in the smallest resolved field in two different grids to parametrize the small-scale stresses with the help of the Smagorinsky eddy-viscosity closure. This procedure is called the dynamic eddy-viscosity model; it introduces several advantages in addition to tuning the model constant. First, the model gives the correct asymptotic behavior near the wall without the use of *ad hoc* wall-damping functions. Second, the SGS stresses vanish in the laminar-flow region without the use of an *ad hoc* intermittency function. Third, the model allows for backscatter (i.e., the energy transfer from subgrid to large scales). Germano *et al.* [19] have applied the dynamic model to both incompressible channel and boundary-layer flows.

The LES of high-speed flows has recently received increasing interest. For compressible isotropic turbulence, Speziale *et al.* [20] and Erlebacher *et al.* [21] have developed a compressible analog of the linear combination SGS model of Bardina *et al.* [22] (called the SEZH model); Zang *et al.* [23] used this model and found good agreement with the DNS data for three-dimensional compressible turbulence. Normand and Lesieur [24] applied the structure-function model to compressible isotropic turbulence as well as compressible transition. Kral and Zang [25] performed an LES of a Mach 4.5 turbulent boundary layer with the structure-function model; Zang *et al.* [26] performed an LES of a Mach 4.5 transitional boundary layer. Both used a compressible analog of the structure-function model with the addition of wall damping and intermittency terms; they obtained better agreement with experiment in comparison with the modified Smagorinsky model. Moin *et al.* [27] have extended the dynamic model of Germano *et al.* to compressible flows and scalar transport and applied it to the LES of decaying isotropic turbulence. El-Hady *et al.* [28] have established the feasibility of using the dynamics SGS model in the LES of high-speed transitional flows.

In this paper we study the nonlinear evolution and breakdown to turbulence of the laminar boundary layer in high-speed flows, as well as the structure of the flow field during the transition process. This study is achieved by using state-of-the-art SGS modeling in a large-eddy temporal simulation, where the large flow structures are computed and the small scales are dynamically modeled. The DNS of Pruett and Zang [29] is used as a means of validation, hence, the same flow field is used in this study; it is the transitional axial flow field on an axisymmetric body (a hollow cylinder) at a Mach number of 4.5 and at a Reynolds number of 10,000, based on the boundary-layer displacement thickness. In the remainder of this paper we introduce the governing equations, develop the Smagorinsky-based SGS dynamic model, and present the numerical procedures for the LES. We then discuss the results of the LES for a transitional boundary layer at a Mach number of 4.5 and introduce a dynamic model that utilizes the structure function. Finally, we close with some concluding remarks.

2. Problem Formulation

Governing Equations

The three-dimensional compressible Navier–Stokes and energy equations describe the axisymmetric flow field along a cylinder of radius R_a^*. The equations are written in the body-fitted coordinate system x, y, z, where x is the direction along the body, y is the normal to the body, and z is the azimuthal direction. The boundary-layer displacement thickness δ^*, the edge velocity u_e^*, δ^*/u_e^*, and $\rho_e^* u_e^{*2}$ are used to make dimensionless lengths, velocities, time, and pressure, respectively. The

temperature, density, specific heats, viscosity, and thermal conductivity of air are made dimensionless with their corresponding edge values. The displacement thickness δ^* is defined for the axisymmetric boundary layer by the quadratic equation

$$\delta^*\left[1+\frac{\delta^*}{2R_a^*}\right]=\int_0^\infty \frac{r^*}{R_a^*}\left[1-\frac{\rho^* u^*}{\rho_e^* u_e^*}\right]dy^*, \tag{1}$$

where r^* is the radial coordinate defined as $r^*(y)=R_a^*+y^*$. Equation (1) reduces to the standard planar boundary-layer definition as $R_a^*\to\infty$. In terms of these dimensionless quantities, the governing equations in vectorial form read

$$\frac{\partial\rho}{\partial t}+\nabla\cdot(\rho\mathbf{V})=0, \tag{2}$$

$$\frac{\partial(\rho\mathbf{V})}{\partial t}+\nabla\cdot(\rho\mathbf{V}\mathbf{V})+\mathbf{\Lambda}=-\nabla p+\frac{1}{R}\nabla\cdot\boldsymbol{\sigma}+\boldsymbol{\chi}, \tag{3}$$

$$\frac{\partial p}{\partial t}+\mathbf{V}\cdot\nabla p+\gamma p\nabla\cdot\mathbf{V}=\frac{1}{M_e^2\Gamma R}\nabla\cdot(k\nabla\theta)+\frac{\gamma-1}{R}\mathbf{\Phi}, \tag{4}$$

with the state equation for an ideal gas

$$\gamma M_e^2 p=p\theta. \tag{5}$$

In the above equations, $\boldsymbol{\sigma}$ is the dimensionless viscous stress tensor, and $\mathbf{\Phi}$ is the dimensionless dissipation function. They are defined as

$$\boldsymbol{\sigma}=\mu[\nabla\mathbf{V}+(\nabla\mathbf{V})^{\mathrm{T}}]+\lambda(\nabla\cdot\mathbf{V})\mathbf{I}, \tag{6}$$

$$\mathbf{\Phi}=\boldsymbol{\sigma}:\nabla\mathbf{V}. \tag{7}$$

Also, in this coordinate system, the vector operators are defined as

$$\nabla\cdot\mathbf{V}\equiv\frac{\partial u}{\partial x}+\frac{R_a}{r}\frac{\partial w}{\partial z}+\frac{\partial v}{\partial y}+\frac{v}{r}, \tag{8}$$

$$\mathbf{V}\cdot\nabla p\equiv u\frac{\partial p}{\partial x}+\frac{R_a}{r}w\frac{\partial p}{\partial z}+v\frac{\partial p}{\partial y}, \tag{9}$$

and some extra terms $\mathbf{\Lambda}$ and $\boldsymbol{\chi}$ appear in the momentum equation; these are defined as

$$\mathbf{\Lambda}\equiv-\frac{\rho w}{r}(0,\,v,\,-w), \tag{10}$$

$$\boldsymbol{\chi}\equiv-\frac{1}{rR}(0,\,\sigma_{zy},\,\sigma_{zz}). \tag{11}$$

Here, γ is the ratio of specific heats ($\gamma=1.4$); M_e is the edge Mach number; $R=\rho_e u_e\delta^*/\mu_e$ is the Reynolds number; $\Gamma=c_p\mu_e/k_e$ is the Prandtl number ($\Gamma=0.72$); μ and λ are the first and second coefficients of viscosity, respectively; k is the thermal conductivity; $\mathbf{I}$ is a unit tensor; and $(\ )^{\mathrm{T}}$ denotes a transpose. The Stokes hypothesis is assumed, and the viscosity and thermal conductivity are related to the temperature θ through Sutherland's law.

Instead of solving (2)–(5) directly for the full range of scales, we limit the resolvable scale size by explicitly applying the spatial filter G to each term in the Navier–Stokes and energy equations. This filtering process will separate the resolvable field from the SGS field, which is accomplished by decomposing each field quantity F in the flow domain D as

$$F=\bar{F}+F'', \tag{12}$$

where the filtered quantity $\bar{F}$ is defined as

$$\bar{F}(\mathbf{x},\,t)=\int_D G(\mathbf{x}-\zeta,\,\Delta)F(\zeta,\,t)\,d\zeta \tag{13}$$

and F'' is the SGS part that accounts for those scales not resolved by the filter width Δ. We note here that the filtered quantity $\bar{F}$ in (12) is a spatially averaged, time-dependent resolved quantity, rather than a time-averaged or ensemble-averaged mean quantity as in the Reynolds-averaged Navier–Stokes (RANS) equations. We keep Δ as a parameter in the integral (13) to show clearly that the computed large-scale field and, consequently, the computed SGS field depend on the filter width. The smallest scale allowed by the filter and the SGS model, which is $O(\Delta)$, should be greater than the smallest scale resolved by the grid size, which is $O(h)$. This relationship will ensure that the computations are independent of the numerical algorithm used in the simulations. In these calculations we choose the filter width $\Delta_i = 2h_i$, where h_i is the grid size in the ith direction.

We use a sharp Fourier cutoff filter (the appropriate choice in a spectral simulation) and apply it in the wave space; it is conveniently defined as

$$\hat{G}_i(k_i) = \begin{cases} 1 & \text{for} \quad k_i \le K_{ci}, \\ 0 & \text{otherwise}, \end{cases} \tag{14}$$

where $\hat{G}_i$ is the Fourier coefficient of the filter function in the ith direction and K_{ci} is the cutoff wave number in the ith direction (related to the corresponding filter width Δ_i by $K_{ci} = \pi/\Delta_i$).

To account for large density fluctuations in high-speed flows, the resolved velocity and temperature fields are written in terms of Favre-filtered quantities [20], which are defined as

$$\tilde{F} = \frac{\overline{\rho F}}{\bar{\rho}}. \tag{15}$$

Now F is decomposed to

$$F = \tilde{F} + F', \tag{16}$$

where F' is the SGS part of F, based on Favre filtering; consequently, the Favre-filtered governing equations used for the LES are

$$\frac{\partial \bar{\rho}}{\partial t} + \nabla \cdot (\bar{\rho}\tilde{\mathbf{V}}) = 0, \tag{17}$$

$$\frac{\partial (\bar{\rho}\tilde{\mathbf{V}})}{\partial t} + \nabla \cdot (\bar{\rho}\tilde{\mathbf{V}}\tilde{\mathbf{V}}) + \bar{\Lambda} = -\nabla \bar{p} + \frac{1}{R}\nabla \cdot \bar{\boldsymbol{\sigma}} - \nabla \cdot \boldsymbol{\tau} + \bar{\chi}, \tag{18}$$

$$\frac{\partial \bar{p}}{\partial t} + \tilde{\mathbf{V}} \cdot \nabla \bar{p} + \gamma \bar{p} \nabla \cdot \tilde{\mathbf{V}} = (\gamma - 1)(\overline{\mathbf{V} \cdot \nabla p} - \tilde{\mathbf{V}} \cdot \nabla \bar{p}) + \frac{1}{M_e^2 \Gamma R}\nabla \cdot (\overline{k \nabla \theta}) + \frac{\gamma - 1}{R}\bar{\Phi} - \frac{1}{M_e^2}\nabla \cdot \mathbf{q}, \tag{19}$$

with the state equation

$$\gamma M_e^2 \bar{p} = \bar{\rho}\tilde{\theta}. \tag{20}$$

In deriving (17)–(20), we have utilized the commutative property of the filtering process with space and time such that

$$\frac{\overline{\partial F}}{\partial t} = \frac{\partial \bar{F}}{\partial t}, \qquad \overline{\nabla \cdot F} = \nabla \cdot \bar{F}. \tag{21}$$

Also, we have decomposed the stress tensor $\bar{\rho}\widetilde{\mathbf{V}\mathbf{V}}$ into its resolved $\bar{\rho}\tilde{\mathbf{V}}\tilde{\mathbf{V}}$ and SGS components $\boldsymbol{\tau}$ and the heat flux $\bar{\rho}\widetilde{\mathbf{V}\theta}$ into its resolved $\bar{\rho}\tilde{\mathbf{V}}\tilde{\theta}$ and SGS components $\mathbf{q}$. Also, in the filtering process, the extra term $\bar{\Lambda}$ that results from the use of a body-fitted coordinate system will contribute to the SGS; it is now defined as

$$\bar{\Lambda} = -\frac{\bar{\rho}\tilde{w}}{r}(0, \tilde{v}, -\tilde{w}) - \frac{1}{r}(0, \tau_{zy}, -\tau_{zz}). \tag{22}$$

The viscous terms in the momentum and energy equations, and the pressure dilatation and conduction terms in the energy equations, need special treatment. In accordance with Erlebacher *et al.* [21] and Zang *et al.* [23], we further simplify (17)–(20) by assuming that $\bar{\boldsymbol{\sigma}} = \boldsymbol{\sigma}(\tilde{\mathbf{V}})$, $(\gamma - 1) \times (\overline{\mathbf{V} \cdot \nabla p} - \tilde{\mathbf{V}} \cdot \nabla \bar{p}) = 0$, $\overline{k \nabla \theta} = \bar{k} \nabla \tilde{\theta}$, $\bar{\boldsymbol{\Phi}} = \boldsymbol{\Phi}(\tilde{\mathbf{V}})$, and neglecting the contribution to the SGS by the viscous dissipation.

The SGS stress tensor τ and the SGS heat-flux vector $\mathbf{q}$ appear in the right-hand side of the momentum and energy equations, respectively; they must be modeled to close these equations. The SGS stress tensor τ consists of the Leonard, cross, and Reynolds stresses, which are defined as

$$L_{kl} = \bar{\rho}(\widetilde{\tilde{u}_k \tilde{u}_l} - \tilde{u}_k \tilde{u}_l), \tag{23}$$

$$C_{kl} = \bar{\rho}(\widetilde{u_k' \tilde{u}_l} + \widetilde{\tilde{u}_k u_l'}), \tag{24}$$

$$R_{kl} = \bar{\rho}(\widetilde{u_k' u_l'}). \tag{25}$$

The SGS heat-flux vector $\mathbf{q}$ consists of similar components, which are defined as

$$qL_k = \bar{\rho}(\widetilde{\tilde{u}_k \tilde{\theta}} - \tilde{u}_k \tilde{\theta}), \tag{26}$$

$$qC_k = \bar{\rho}(\widetilde{u_k' \tilde{\theta}} + \widetilde{\tilde{u}_k \theta'}), \tag{27}$$

$$qR_k = \bar{\rho}(\widetilde{u_k' \theta'}). \tag{28}$$

Supplemented with appropriate initial and boundary conditions, (17)–(20) are used to yield the resolved flow field for all later times.

Modeling the Small-Grid Scales

To model the SGS stress tensor τ and the SGS heat-flux vector $\mathbf{q}$, we use the approach given by Speziale *et al.* [20] and Erlebacher *et al.* [21], which is based on the compressible extension of the eddy-viscosity Smagorinsky model [9] and an analogous eddy diffusivity model; these are modeled as

$$\tau_{kl} = \bar{\rho}(\widetilde{\tilde{u}_k \tilde{u}_l} - \tilde{\tilde{u}}_k \tilde{\tilde{u}}_l) - 2C_r \bar{\rho} \Delta^2 |\tilde{S}| \tilde{S}_{kl}' + \tfrac{2}{3} C_i \bar{\rho} \Delta^2 |\tilde{S}|^2 \delta_{kl}, \tag{29}$$

$$q_k = \bar{\rho}(\widetilde{u_k \tilde{\theta}} - \tilde{\tilde{u}}_k \tilde{\tilde{\theta}}) - C_\theta \bar{\rho} \Delta^2 |\tilde{S}| \frac{\partial \tilde{\theta}}{\partial x_k}, \tag{30}$$

where δ_{kl} is the Kronecker delta. The characteristic grid filter with Δ and the Favre-filtered rate-of-strain tensor $\tilde{S}_{kl}$ are defined as

$$\Delta = (\Delta_x \Delta_y \Delta_z)^{1/3}, \tag{31}$$

$$\tilde{S}_{xx} = \frac{\partial \tilde{u}}{\partial x}, \tag{32a}$$

$$\tilde{S}_{xz} = \tfrac{1}{2}\left(\frac{R_a}{r}\frac{\partial \tilde{u}}{\partial z} + \frac{\partial \tilde{w}}{\partial x}\right), \tag{32b}$$

$$\tilde{S}_{xy} = \tfrac{1}{2}\left(\frac{\partial \tilde{u}}{\partial y} + \frac{\partial \tilde{v}}{\partial x}\right), \tag{32c}$$

$$\tilde{S}_{zz} = \frac{R_a}{r}\frac{\partial \tilde{w}}{\partial z} + \frac{\tilde{v}}{r}, \tag{32d}$$

$$\tilde{S}_{zy} = \tfrac{1}{2}\left(\frac{R_a}{r}\frac{\partial \tilde{v}}{\partial z} + \frac{\partial \tilde{w}}{\partial y} - \frac{\tilde{w}}{r}\right), \tag{32e}$$

$$\tilde{S}_{yy} = \frac{\partial \tilde{v}}{\partial y}, \tag{32f}$$

and

$$\tilde{S}_{kl}' = \tilde{S}_{kl} - \tfrac{1}{3}\tilde{S}_{kk}\delta_{kl}, \tag{33}$$

$$|\tilde{S}| = (2\tilde{S}_{kl}\tilde{S}_{kl})^{1/2}. \tag{34}$$

Note that the first term in (29) and (30) represents the scale similarity part of the model; it is the sum of the Leonard and cross portions of the SGS stress or heat-flux fields. The remaining parts of the equations represent the model for the Reynolds portion of the stress, the SGS energy (the isotropic

part), and the heat-flux fields. Piomelli *et al.* [30] indicated the need for the model to be consistent with the type of filter used in any analysis and with the cutoff filter, the scale similarity portion of the model is neglected. Here, we model the SGS field by the eddy-viscosity and its analogous eddy-diffusivity portions, and neglect the scale similarity. The coefficients of the model C_r, C_i, and C_θ are to be determined.

Smagorinsky-Based Dynamic Model

In accordance with the dynamic procedure for SGS modeling [19], we apply a second filter to the equations of motion (17)–(20). We use, again, a sharp Fourier cutoff filter and apply it in the wave space (see (14)). The second filter width $\hat{\Delta}_i$ in the ith direction is larger that the first filter width Δ_i in the same direction. The ratio $\eta = \hat{\Delta}_i/\Delta_i = 2$ is adopted in the present calculations. The second filter has the characteristic width

$$\hat{\Delta} = (\eta\Delta_x\Delta_y\eta\Delta_z)^{1/3}. \tag{35}$$

The sharp Fourier cutoff filter is applied in the two periodic directions along the body and in the azimuthal direction where the grid is uniform; no filter is applied in the direction normal to the wall. Filtering in this direction requires the use of a nonuniform filter width which invalidate the LES equations (17)–(20); the filtering operation will not commute with spatial differentiation. This difficulty is currently under intense investigation, and was addressed recently by Gosal and Moin [31]. The first and second filters, usually called grid and test filters, respectively, each produce a resolved flow field. The difference between the two resolved fields is the contribution by the small scales of length between the grid- and test-filter widths.

The SGS stresses and heat flux that appear in (18) and (19) can be defined as

$$\tau_{kl} = \bar{\rho}(\widetilde{u_k u_l} - \tilde{u}_k\tilde{u}_l), \tag{36}$$

$$q_k = \bar{\rho}(\widetilde{u_k\theta} - \tilde{u}_k\tilde{\theta}). \tag{37}$$

Analogous to the above equations, the SGS stresses and heat flux that appear in the test-filtered equations can be defined as

$$T_{kl} = \hat{\bar{\rho}}(\widehat{\widetilde{u_k u_l}} - \hat{\tilde{u}}_k\hat{\tilde{u}}_l), \tag{38}$$

$$Q_k = \hat{\bar{\rho}}(\widehat{\widetilde{u_k\theta}} - \hat{\tilde{u}}_k\hat{\tilde{\theta}}). \tag{39}$$

By assuming the same functional form and model coefficients, the test-filtered SGS stresses and heat flux are modeled the same way as in (29) and (30), with the scale similarity portion neglected, as

$$T_{kl} = -2C_r\hat{\bar{\rho}}\hat{\Delta}^2|\hat{\tilde{S}}|\hat{\tilde{S}}_{kl} + \tfrac{2}{3}C_i\hat{\bar{\rho}}\hat{\Delta}^2|\hat{\tilde{S}}|^2\delta_{kl}, \tag{40}$$

$$Q_k = -C_\theta\hat{\bar{\rho}}\hat{\Delta}^2|\hat{\tilde{S}}|\frac{\partial\hat{\tilde{\theta}}}{\partial x_k}. \tag{41}$$

The grid-filtered SGS field and the test-filtered SGS field are related by the Germano identity [18], such that

$$D_{kl} \equiv T_{kl} - \hat{\tau}_{kl} = \widehat{\bar{\rho}\tilde{u}_k\tilde{u}_l} - \frac{\hat{\bar{\rho}}\hat{\tilde{u}}_k\hat{\bar{\rho}}\hat{\tilde{u}}_l}{\hat{\bar{\rho}}}, \tag{42}$$

$$E_k \equiv Q_k - \hat{q}_k = \widehat{\bar{\rho}\tilde{u}_k\tilde{\theta}} - \frac{\hat{\bar{\rho}}\hat{\tilde{u}}_k\hat{\bar{\rho}}\hat{\tilde{\theta}}}{\hat{\bar{\rho}}}, \tag{43}$$

where D_{kl} and E_k are computable from the resolved large-eddy field. They are the resolved components of the stress tensor with scales of motion between the test and the grid scales. Lilly [32] called it the test window.

By using the traces of (29), (40), and (42), the following expression can be derived to solve for C_i:

$$D_{kk} = 2C_i(\hat{\Delta}^2\hat{\bar{\rho}}|\hat{\tilde{S}}|^2 - \Delta^2\widehat{\bar{\rho}|\tilde{S}|^2}) \equiv C_iB. \tag{44}$$

By substituting (29), (40), and (44) into (42) and (30) and (41) into (43), the following expressions can

be derived to solve for C_r and C_θ:

$$D_{kl} - \tfrac{1}{3}D_{kk}\delta_{kl} = -2C_r(\hat{\Delta}^2\hat{\bar{\rho}}|\hat{\tilde{S}}|\hat{\tilde{S}}'_{kl} - \Delta^2\widehat{\bar{\rho}|\tilde{S}|\tilde{S}'_{kl}}) \equiv C_r M_{kl}, \tag{45}$$

$$E_k = -C_\theta\left(\hat{\Delta}^2\hat{\bar{\rho}}|\hat{\tilde{S}}|\frac{\partial\hat{\tilde{\theta}}}{\partial x_k} - \Delta^2\widehat{\bar{\rho}|\tilde{S}|\frac{\partial\tilde{\theta}}{\partial x_k}}\right) \equiv C_\theta N_k. \tag{46}$$

Each of the expressions (45) and (46) represents a set of independent equations in one unknown. In order to determine uniquely the model coefficients C_r and C_θ, we use the strain-rate contractions proposed by Germano *et al.* [19] and Moin *et al.* [27] in which (45) is contracted with $\tilde{S}_{kl}$ and (46) is contracted with $\partial\tilde{\theta}/\partial x_k$. We also use another contraction obtained from the least-squares analysis of Lilly [32] in which (45) is contracted with M_{kl} and (46) is contracted with N_k. The first and second contractions are referred to as c_1 and c_2, respectively, in our calculations.

The model coefficients in expressions (44), (45), and (46) are functions of space and time. They can locally become negative, which allows for backscatter (i.e., the transfer of energy from the SGS to the large scale). In their DNS calculations of transitional and turbulent channel flows, Piomelli *et al.* [33] have shown that about half of the grid points experience a backscatter when a Fourier cutoff filter is used. In this simulation, like others using dynamic modeling [19], [27], numerical instability is observed caused by ill-conditioned local values of the model coefficients. To alleviate this numerical instability we assume the model coefficients to be functions only of time and the inhomogeneous direction (the wall-normal direction) and average over the other two homogeneous periodic directions (this is called plane averaging or parallel-to-the-wall averaging and is indicated by $\langle\ \rangle$). Clearly, plane averaging enhances the numerical stability of the simulations at the expense of losing some of the conceptual advantages of the dynamic modeling formulation. Plane averaging leads to the following expressions for the model coefficients:

$$C_i = \frac{\langle D_{kk}\rangle}{\langle B\rangle}, \tag{47}$$

$$C_r = \frac{\langle (D_{kl} - D_{kk}\delta_{kl}/3)\chi_{kl}\rangle}{\langle M_{kl}\chi_{kl}\rangle}, \tag{48}$$

$$C_\theta = \frac{\langle E_k\Lambda_k\rangle}{\langle N_k\Lambda_k\rangle}, \tag{49}$$

where χ_{kl} and Λ_k assume the value given by the type of contraction. With the calculation of the model coefficients, (29) and (30) are used to calculate the SGS stresses and the heat flux to close the governing equations (17)–(20).

3. Numerical Procedures for Large-Eddy Simulations

The solution of (17)–(20) uses basically the same algorithm used by Erlebacher and Hussaini [34] to simulate compressible flow over a flat plate, and by Pruett and Zang [29] to simulate compressible flow over axisymmetric bodies. Here, we briefly describe the main features of the algorithm.

Because the parallel mean flow does not satisfy the governing equations (17)–(20), forcing terms, similar to those given in [34], are added to the right-hand side of these equations to suppress the temporal evolution of the unperturbed mean flow, so that the laminar state becomes stationary. The initial value problem defined by (17)–(20) is explicitly integrated in time by using a third-order low-storage Runge–Kutta method. The time step is automatically controlled by the minimum of the maximum time steps allowed by the linearized advection and diffusion problems. The streamwise and the azimuthal directions are periodic so that the flow variables can be represented by Fourier series in these directions. The periodicity lengths in the streamwise and azimuthal directions ($2L_x$ and L_z) are related to the corresponding wave numbers α and β by $L_x = 2\pi/\alpha$ and $L_z = 2\pi/\beta$. The spatial derivatives in these directions are evaluated at each time step by spectral collocation methods. In the wall-normal direction a sixth-order compact difference scheme is implemented. To increase the

resolution requirements in the direction normal to the wall without drastically decreasing the time step in an explicit scheme, Pruett and Zang [29] have implemented a sixth-order compact-difference scheme in the wall-normal direction instead of the Chebychev collocation method used by Erlebacher and Hussaini [34].

The grid is uniform in the x- and z-directions; a mapping is used in the y-direction, which clusters points near the wall and the critical layer and stretches the grid toward the far-field boundary ($y_{\max} = 15$). Symmetry is enforced about the plane $z = 0$ to reduce the number of grid points in the spanwise direction by half and save computational time. Spectral methods are known to introduce both truncation and aliasing errors. To minimize these errors, we adopted the same method as in [29]; we check the decay of the spectrum of the Fourier coefficients and refine the grid accordingly as necessary.

Equations (47)–(49) are used to evaluate the model coefficients at each time step from the flow field at the previous time step. The SGS stresses and heat flux are evaluated with (29) and (30) at each time step and added to the right-hand side before the governing equations are advanced in time.

At each time step, the energy content $E_{\alpha\beta}$ in any Fourier mode (α, β), normalized with the mean-flow energy E_0, is calculated from the Fourier coefficients of the velocity $\hat{\mathbf{v}}_{\alpha,\beta}$ as

$$E_{\alpha,\beta}(t) = \frac{d_\alpha d_\beta}{2E_0} \int_0^{y_{\max}} \bar{\rho}(y) |\hat{\mathbf{v}}_{\alpha,\beta}(y, t)|^2 \frac{r(y)}{R_a}\, dy,$$

$$d_k = 2 - \delta_{k0}. \tag{50}$$

Simulations are carried out for the flow along a cylinder with a Mach number of 4.5, a stream temperature of 110 °R at the edge of the boundary layer, and at a streamwise station that corresponds to $R = 10{,}000$.

The initial conditions for the temporal numerical simulation match those of the DNS of [29] for the purpose of comparison. They consist of the mean flow along a cylinder $q_0(y)$, an axisymmetric second-mode primary disturbance $q_1(x, y, t)$, and a secondary subharmonic disturbance $q_2(x, y, z, t)$. The mean flow is a spectral solution of the axisymmetric compressible boundary layer [35]. The solution of the primary disturbance assumes the form

$$q_1(x, y, t) = \varepsilon_1 [\tilde{q}_1(y) e^{i(\alpha x - \omega t)} + cc], \tag{51}$$

and the solution of the secondary disturbance assumes the form

$$q_2(x, y, z, t) = \varepsilon_2 [e^{i\alpha(x - \omega t/\alpha)2} e^{i\beta R_a z} \sum_{n=-N}^{N} \tilde{q}_{2,n}(y) e^{in\alpha(x - \omega t/\alpha)} + cc], \tag{52}$$

where $\alpha = 2.523$ and $\omega = 2.285 + i3.19 \times 10^{-3}$ are, respectively, the real wave number and the complex frequency of a primary disturbance of amplitude $\varepsilon_1 = 0.085$. The secondary disturbance has four wave components ($N = 4$), an azimuthal wave number $\beta = 2.09$, and an amplitude $\varepsilon_2 = 0.017$. The eigenfunctions of both the primary and secondary disturbances are normalized such that their amplitudes measure the maximum root-mean-square value of the corresponding temperature disturbance.

Dirichlet boundary conditions are applied to the total flow (except density) at the wall and at the far field. The density is calculated by projecting forward in time with the Runge–Kutta integrator, and the state equation is used to calculate the pressure. The thermal boundary condition used in [29] is adopted here for the purpose of comparison; it is a combination of an adiabatic wall condition for the mean flow and Dirichlet thermal condition for the total flow.

It is necessary to mention a few details about the DNS data of Pruett and Zang [29] that we use here for comparison. The initial resolution of the DNS data at time $t = 0$ was $12 \times 96 \times 6$ (symmetry was enforced about the plane $z = 0$). As time evolves, the streamwise and azimuthal grid refinements were made as necessary to maintain at least a difference of eight orders of magnitude between the most- and the least-energetic Fourier harmonics. A well-resolved flow field was reached for 55 periods of the primary disturbance, with a resolution of $96 \times 144 \times 48$ beyond which the simulation became increasingly ill-resolved.

4. Results of Large-Eddy Simulations

Features of Smagorinsky-Based Dynamic Model

An LES is conducted with the dynamic model and the initial grid $24 \times 96 \times 12$ by using the contraction c_2 (the number of points cited for the spanwise direction, 12 in this case, is half the number for the symmetric full span). The grid is fixed at $24 \times 96 \times 12$ throughout the transition region. Figure 1 shows the time evolution of the dynamic model coefficients C_r, C_i, and C_θ, where time is given in periods of the primary disturbance. Although the coefficients are functions of y and t, they are averaged in the wall-normal direction for the purpose of this graph. The figure illustrates one of the favorable characteristics of the dynamic model; it turns itself off and on without the need for any added *ad hoc* functions. The model is turned off in the linear and weakly nonlinear regions. These regions are recognized in accordance with the development of the primary and secondary disturbances; the linear region is between the periods 0 and 15, and the weakly nonlinear region follows until period 35. The model turns itself on in the strong nonlinear region (from periods 35 to 45). The value of the model coefficients gradually increases as the laminar breakdown commences, continues to increase through the transition region, and then decreases again in the fully turbulent region.

A second LES is conducted in which a grid of $24 \times 96 \times 12$ is used at the initial stages, and is refined as necessary to maintain at least a difference of four orders of magnitude between the most- and the least-energetic Fourier harmonics. The final grid reached is $48 \times 96 \times 24$. The time evolution of the dynamic model coefficients C_r, C_i, and C_θ (averaged in y) is included in Figure 1 for comparison with the first LES of grid $24 \times 96 \times 12$. Further grid refinement in LES reduces the values of the model coefficients; their values become zero as we approach the limit of the DNS grid.

The SGS coefficients are essentially zero in the earlier stages of the transition process, i.e., the primary and secondary instability stages. This means that LES performs the same as DNS at these stages. To double check and assess the accuracy of the numerical method, El-Hady *et al.* [36]

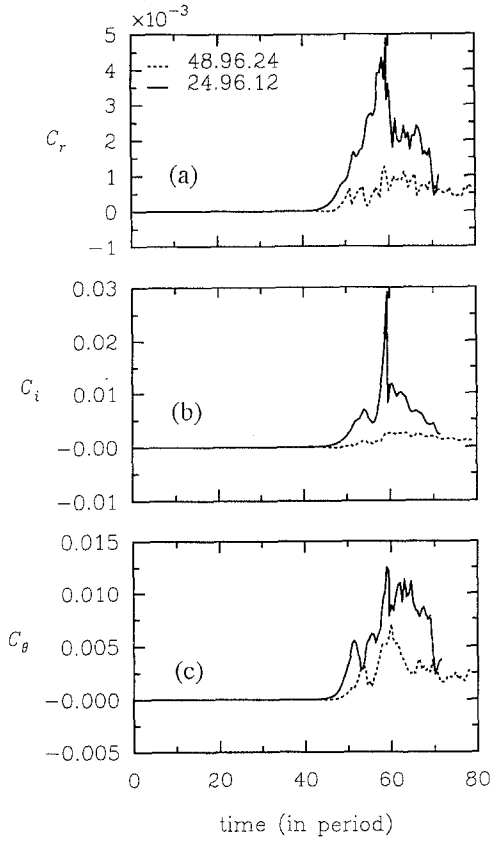

Figure 1. Evolution in time of plane-averaged coefficients of the dynamic model with contraction c_2: (a) C_r, (b) C_i, and (c) C_θ. Coefficients are averaged in the wall-normal direction for this graph.

compared the LES results with that of the linear and secondary stability theories in the early (linear) stage, where the grid is 24 × 96 × 12. Eigenvalues were predicted with an accuracy of $O(10^{-5})$, and the amplitude growth of the primary (1, 0) mode and the secondary $(\frac{1}{2}, 1)$ mode compared well with linear theories.

For the LES with final grid 48 × 96 × 24, we examine the evolution of the wall-normal distribution of the model coefficients with time. Figure 2 shows the y-variation of plane-averaged values of C_r, C_i, and C_θ at $t = 45$, $t = 54$, $t = 62$, and $t = 65$, which correspond to nearly the beginning, the middle, the end of the transition region, and the onset of the turbulent region (see Figure 1). Contraction c_1 is used in the simulations to produce Figure 2. The figure shows that the model gives the proper asymptotic behavior near the wall and vanishes in the free stream (without the need for *ad hoc* damping functions). Also, the values of the model coefficients are almost negligible in the linear and early nonlinear stages and increase sharply in the wall region as the breakdown progresses. As the turbulent stage approaches, the values of the model coefficients drop and are not confined to the wall region, but spread away from the wall.

The plane-averaged value of the turbulent Prandtl number Pr_t is defined by the ratio C_r/C_θ. This parameter directly influences the modeling of the SGS heat flux in (30). In the y-region, where both C_r and C_θ have a nonzero value, Figure 3 shows the evolution of the wall-normal distribution of the turbulent Prandtl number with time for the LES with final grid 48 × 96 × 24. The figure indicates that Pr_t reaches an average value of 0.3–0.5 in the transition region (compared with a value of 0.72 used for the laminar Prandtl number). For compressible isotropic turbulence, a value of Pr_t around 0.4 has been predicted by the dynamic model in an LES calculation [27] and an optimal value of about 0.5 was given by others [21]. We note that, although Pr_t varies across the boundary layer, most

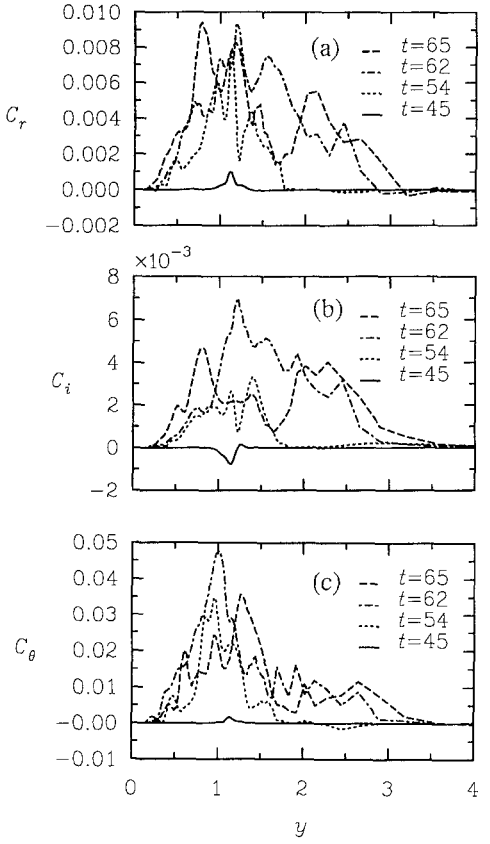

Figure 2. Evolution in time of the normal-to-wall distribution of plane-averaged coefficients of the dynamic model with contraction c_1: (a) C_r, (b) C_i, and (c) C_θ.

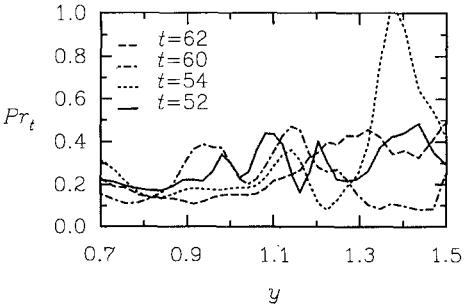

Figure 3. Evolution in time of the normal-to-wall distribution of the plane-averaged turbulent Prandtl number Pr_t with contraction c_1.

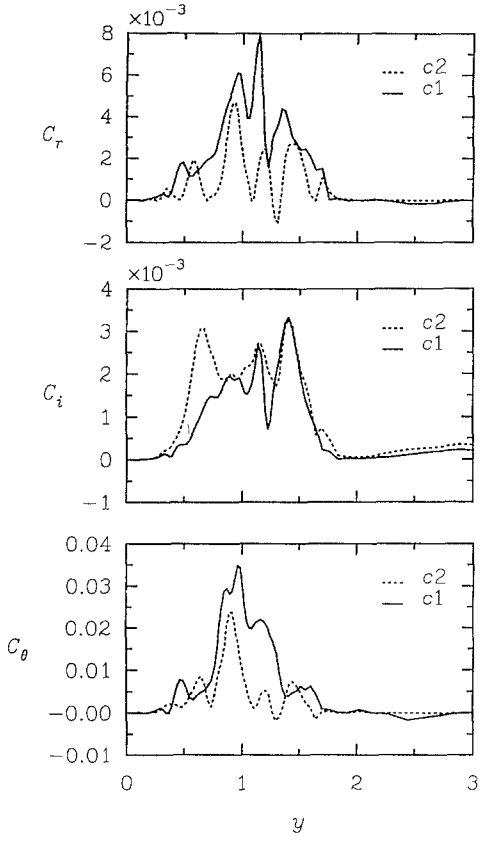

Figure 4. Effect of different contractions on plane-averaged coefficients of the dynamic model at $t = 54$: (a) C_r, (b) C_i, and (c) C_θ.

RANS calculations that use algebraic turbulence models for air take Pr_t as a constant near 1 (most commonly 0.9).

Contraction c_1 was used in the simulations that produced Figure 2. When contraction c_2 is used, similar observations are noted in addition to the reduction by nearly a factor of 2 in the value of the coefficients C_r and C_θ. Figure 4 shows the effect of contraction type on the model coefficients at $t = 54$ for the LES with final grid $48 \times 96 \times 24$. Although the type of contraction does not affect the value of C_i in an *a priori* test [28], an LES does affect their values, most probably because of the interaction between the modeled and large scales. Although the values for C_r and C_θ predicted by the contraction c_2 are lower than those predicted by the contraction c_1, the value of C_i calculated with contraction c_2 is slightly higher than that calculated with contraction c_1 as shown in Figure 4. The variations in the model coefficients due to the type of contraction will directly influence the modeled values of the local SGS stresses and heat flux. However, the local values of the SGS field are not essential to the evolution of the large-scale field. The divergence of the SGS field is the quantity that enters the momentum and energy equations. In a later section we show the effect of contraction type on flow structure.

Global Features of the Flow Field

The effect of the filter width was investigated in an *a priori* test by El-Hady *et al.* [28] by using DNS data inside the transition region. They found that, as the filter width increases (coarser grid), the value of the model coefficients increases, resulting in a sharp rise and high oscillations in the energy contained in the SGS in the wall region. In a full simulation we chose a grid-filter width that is capable of providing the right amount of energy transfer between the large and subgrid scales by checking the kinetic energy spectra and energy content in various Fourier modes. For the LES with a fixed grid at $24 \times 96 \times 12$ throughout the transition region, the one-dimensional kinetic energy spectra is checked against the corresponding spectra of a fine-grid DNS and a coarse-grid DNS (no SGS model). Also, the energy content of some of the principal modes (Fourier harmonics) is checked

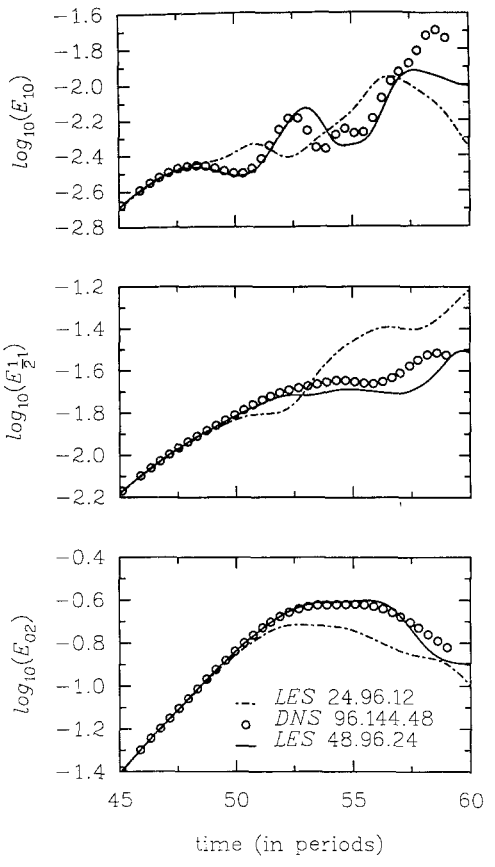

Figure 5. Comparison of the time evolution of the energy content of Fourier harmonics (1, 0), ($\frac{1}{2}$, 1), (0, 2) inside the transition region between LES (24 × 96 × 12), LES (48 × 96 × 24), with contraction c_1, and fine-grid DNS (96 × 144 × 48) [29].

against the corresponding energy content of a fine-grid DNS. These checks demonstrate that the dynamic model with the grid 24 × 96 × 12 is capable of predicting the correct energy content of various Fourier modes only to a stage near the onset of transition (determined here by the rise in wall skin friction).

For the second LES calculations, where we reached a final grid of 48 × 96 × 24, the one-dimensional spectra of the kinetic energy in both the streamwise and spanwise directions exhibits good agreement with the fine-grid DNS. In Figure 5 we show a close comparison inside the transition region between the two LESs presented in this paper (with grids 24 × 96 × 12 and 48 × 96 × 24) with contraction c_1 and the fine-grid DNS 96 × 144 × 48 of Pruett and Zang [29] for the energy content of the principal modes (1, 0), ($\frac{1}{2}$, 1), and (0, 2). As mentioned before, in the case of the dynamic model with the grid 24 × 96 × 12, the good comparison stops near the onset of transition. The dynamic model with the grid 48 × 96 × 24 shows good agreement with the DNS and is capable of predicting the correct energy content of various Fourier modes all the way to and through the transition region. On the other hand, contraction c_2 with the same grid did not do as good as contraction c_1 in predicting the energy content in the dominant Fourier modes especially in the middle of the transition region. More is to be said about that in a coming section.

For the LES calculations with contraction c_1, where we reached a final grid of 48 × 96 × 24, Figure 6 shows the time evolution of the principal Fourier harmonics in terms of its energy content. Of these, three harmonics ((1, 0), ($\frac{1}{2}$, 1), and ($\frac{3}{2}$, 1)) are present in the initial conditions (together with their complex conjugates); however, the others ((0, 2), (1, 2), and (2, 2)) emerged from the self-interaction of different components of the secondary disturbance. The different stages of evolution (linear, weakly nonlinear, strongly nonlinear, and breakdown) are recognized in accordance with the development of the primary mode (1, 0) and the secondary subharmonics ($\frac{1}{2}$, 1) and ($\frac{3}{2}$, 1). The evolution of the various modes agrees well with the fine-grid DNS [29]. Of interest is the LES prediction of the domination of mode (0, 2) near period 30 as indicated by the DNS [29]. The overall

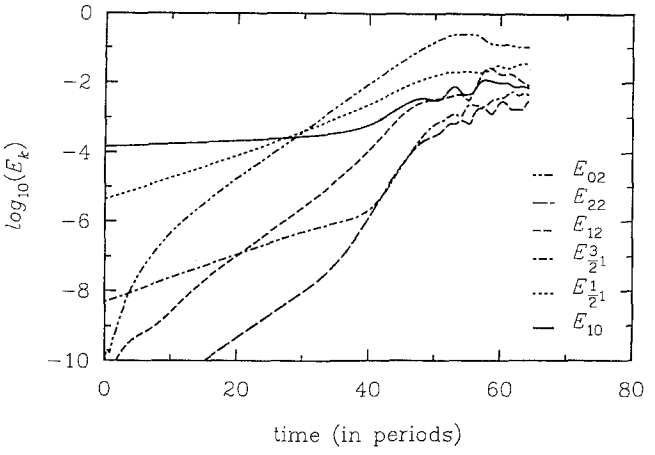

Figure 6. Evolution in time of the principal Fourier harmonics in terms of energy content for LES with final grid 48 × 96 × 24 and contraction c_1.

picture is essentially the same when we use contraction c_2 except that slight variations in the energy content of the Fourier harmonics are observed in the transition region between $t = 50$ and $t = 60$.

Figure 7 shows the development of the resolved field with time. The figure gives the y-variation of the plane-averaged values of the Reynolds stress component τ_{xz}, the kinetic energy K, and the heat-flux component q_z at progressive times. The kinetic energy K is dominated by the component τ_{xx} of the resolved Reynolds stress tensor; the other two components τ_{yy} and τ_{zz} are an order of magnitude less (same as τ_{xz} shown in the figure). Also, q_z is the dominant component of the heat-flux vector at all times. At $t = 45$, all quantities peak near $y = 1$ (the critical layer). As time progresses (e.g., at $t = 54$ inside the transition region) the peak value increases and shifts toward the wall. At $t = 62$,

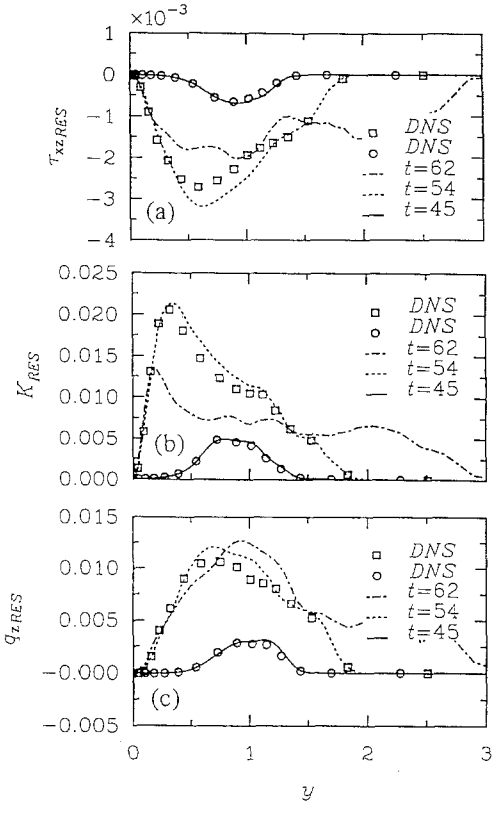

Figure 7. Evolution in time of the large-scale field (resolved) with contraction c_1 in terms of plane-averaged (a) Reynolds stress component τ_{xz}, (b) kinetic energy K, and (c) heat-flux component q_z.

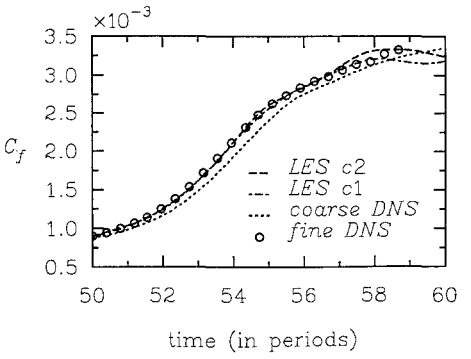

Figure 8. Comparison of time development of the skin friction C_f with contractions c_1 and c_2 with both fine- and coarse-grid DNS results.

the maximum value drops sharply (slower in the case of q_z) with more uniform distribution across the boundary layer, indicating turbulent activities. This reduction in magnitude brings the level down to a value that is typical for turbulent flows. The fluctuations of the resolved Reynolds stresses and heat flux extend well outside the boundary-layer thickness. Figure 7 shows a comparison with the fine-grid DNS results at $t = 45$ and $t = 54$, where the DNS results are filtered on the same grid that is used for the LES. Fine-grid DNS results are not available at $t = 62$.

The time evolution of the plane-averaged skin friction C_f is shown in Figure 8 for the LES with final grid $48 \times 96 \times 24$. The results from both types of contraction are compared with a fine-grid DNS and a coarse-grid DNS. The coarse-grid DNS is the same grid used for LES, but without the SGS modeling. A remakable agreement exists between LES calculations and the fine DNS results, which indicates that the dynamic model ensures the transfer of the correct amount of energy between the large and the subgrid scales. Without the SGS dynamic modeling, the coarse-grid DNS results fail to predict the evolution of the skin friction during the transition region. Notice that both types of contraction used in the LES calculations give the same results until the end of the transition region, where some differences appear. Notice also that meaningful comparison beyond $t = 55$ is in doubt because the fine-grid DNS simulation [29] became increasingly ill-resolved.

The Structure of the Flow Field

The type of instability simulated in this paper leads to a flow-field structure that is dominated by periodic lambda-shaped vortices that are shifted by one-half of a wavelength in the spanwise direction and staggered in the streamwise direction. Figure 9 shows a plan view, just below the critical layer, of the total vorticity predicted by the LES with the contraction c_1 and by the fine-grid DNS at $t = 45$. The figure indicates an excellent prediction of the flow structure by LES at this time. Also, LES is able to capture the "rope-like" wave structure that is derived from the wall-normal density gradient. Figure 10 compares the "rope-like" structure at $t = 45$ with the corresponding structure from the fine-grid DNS of Pruett and Zang [29]. Although a coarse-grid DNS (same as the LES grid) might be able to capture the flow structure at this early time, $t = 45$, it is significant, as Figures 9 and 10 show, that LES with the dynamic model causes no damping to the flow structure during the early stages of transition as does the standard Smagorinsky model [9]. The contraction c_2 gives identical results (not shown). In all comparisons with DNS, including Figures 9 and 10, the DNS grid is filtered to the corresponding LES grid.

Following the periodic lambda-shaped vortices, detached high-shear layers of the streamwise velocity are subsequently developed, which ride on top of the lambda vortices. With the intensity of the high-shear layers increasing, they stretch and eventually roll up. Sharp, low-velocity pulses (spikes) are then observed in the peak positions. At several stages in the transition region ($t = 50$, $t = 53$, $t = 54$, and $t = 55$) we compare the flow structure, in terms of the spanwise vorticity that results from LES calculations, with the DNS results [29]. Figures 11–14 show this comparison for both contractions used in the LES calculations. These figures illustrate several points. First, excellent agreement exists between the LES and DNS results; the LES, with the dynamic model, is able to capture the bulk of the flow structure. Second, both contractions give identical results at the early stages of the transition region (at $t = 50$, the maximum spanwise vorticity is 4.9 for both contractions, compared

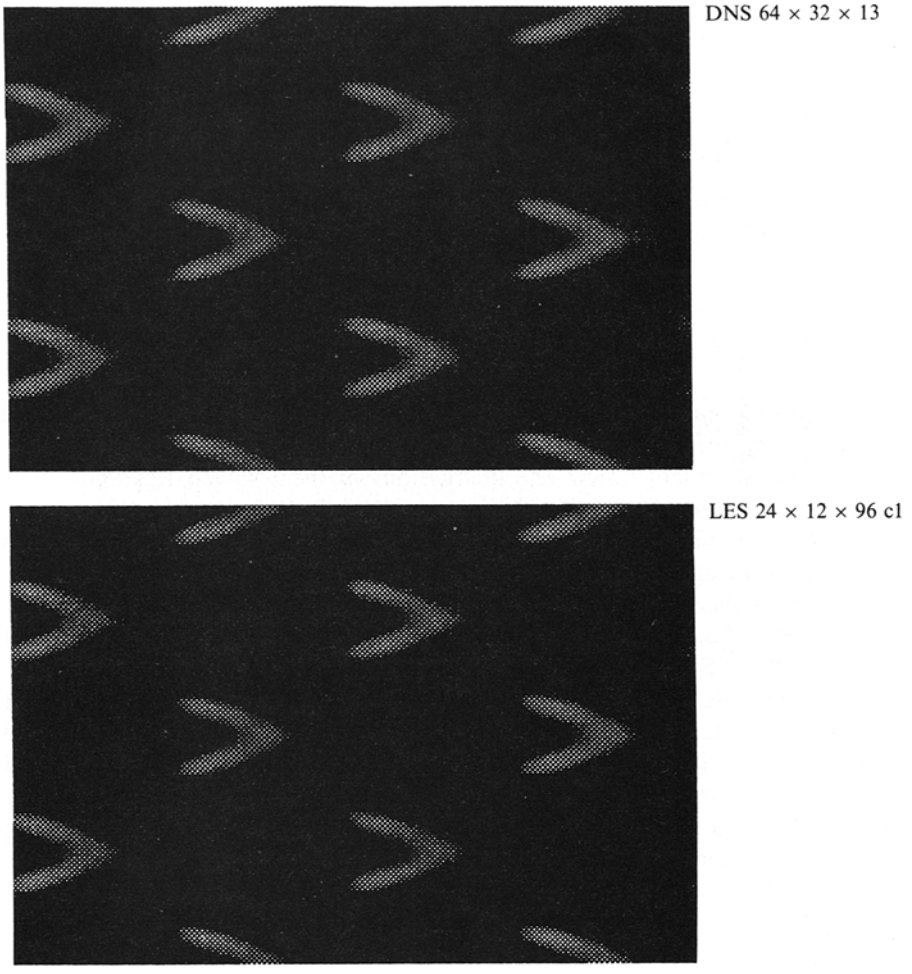

Figure 9. Comparison of total vorticity (plan view just below the critical layer) at $t = 45$ between LES and DNS with fine grid [29].

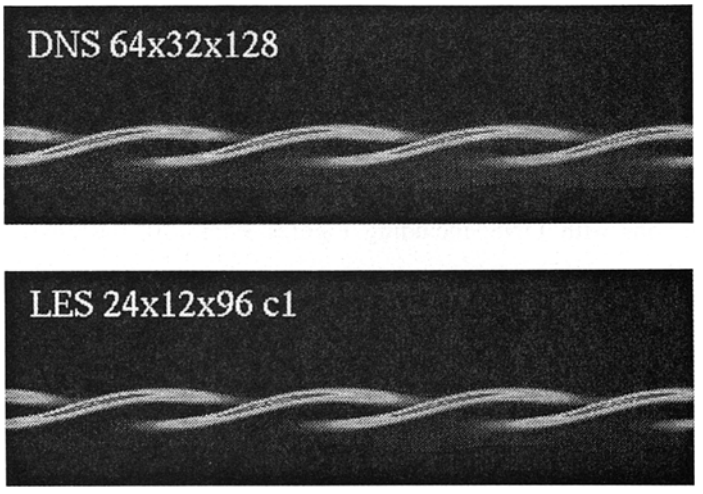

Figure 10. Rope-like structure derived from the wall-normal density gradient at $t = 45$ for LES with grid $24 \times 96 \times 12$ compared with a corresponding structure from DNS with fine grid [29].

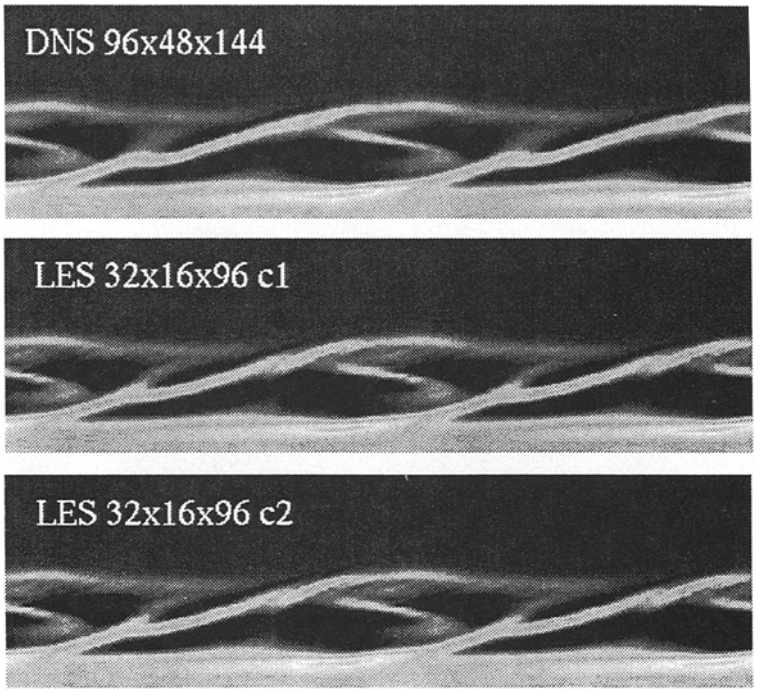

Figure 11. Comparison of the spanwise component of vorticity at $t = 50$ between LES and DNS with fine grid [29].

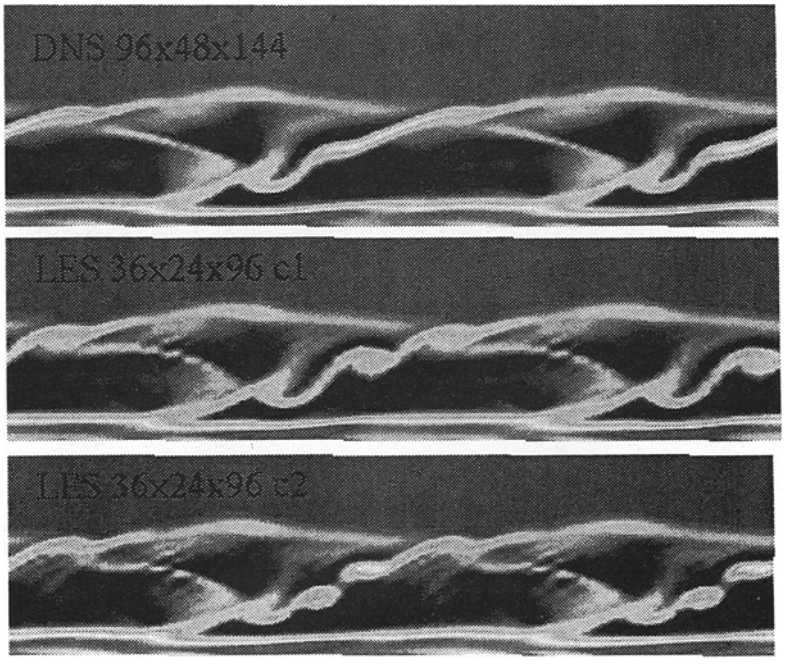

Figure 12. Comparison of the spanwise component of vorticity at $t = 53$ between LES and DNS with fine grid [29].

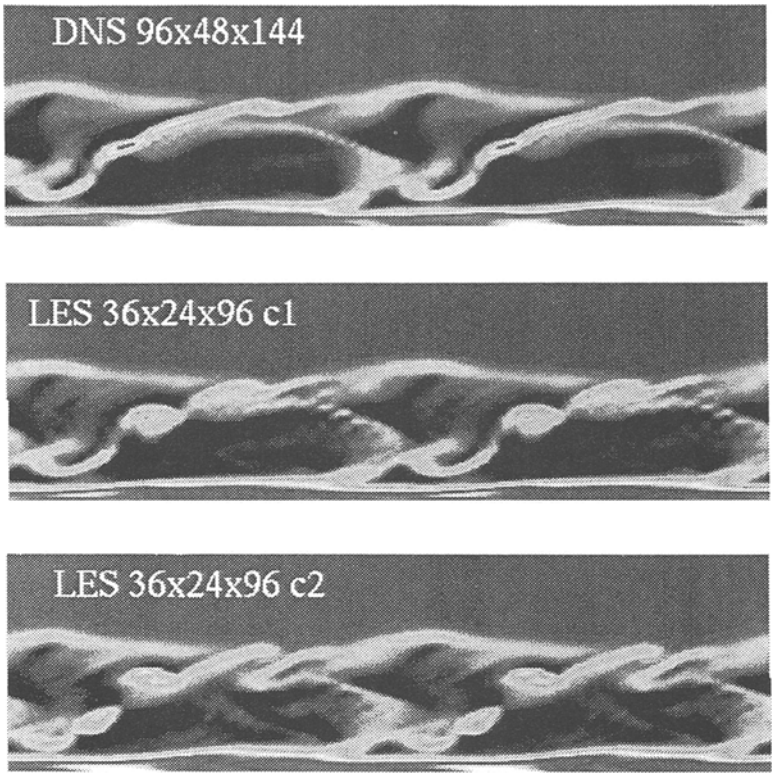

Figure 13. Comparison of the spanwise component of vorticity at $t = 54$ between LES and DNS with fine grid [29].

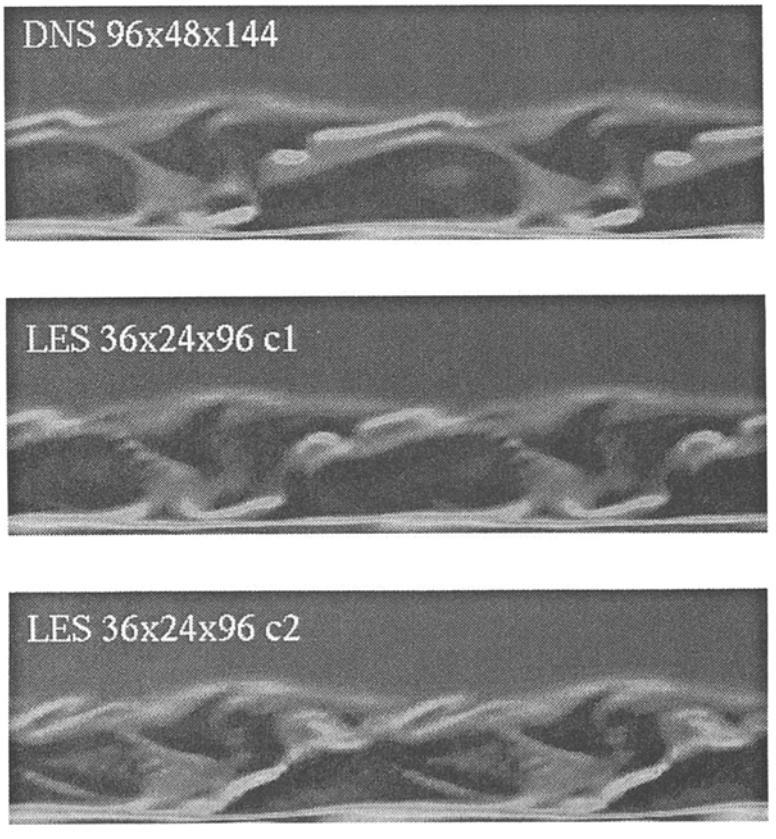

Figure 14. Comparison of the spanwise component of vorticity at $t = 55$ between LES and DNS with fine grid [29].

with 5.1 for DNS). Third, slight differences in the details of the flow structure begin to occur in the late stages of transition. Fourth, at these late stages of transition, the LES flow-field structure with contraction c_1 compares more favorably with the DNS results. In the next section we use a new dynamic model which appears to resolve these differences.

As the transition process continues, small structures are formed due to the breakdown of the high-shear layer. This results in the periodical appearance of local regions of turbulence in the streamwise and spanwise directions. These regions spread as they travel downstream until a fully turbulent flow is attained. The later developments of the flow field are never understood in high-speed flows because of rare DNS calculations that cover the high computer demand of this stage. In Figure 15 we present the results of the LES with contraction c_1; these results describe the spanwise vorticity

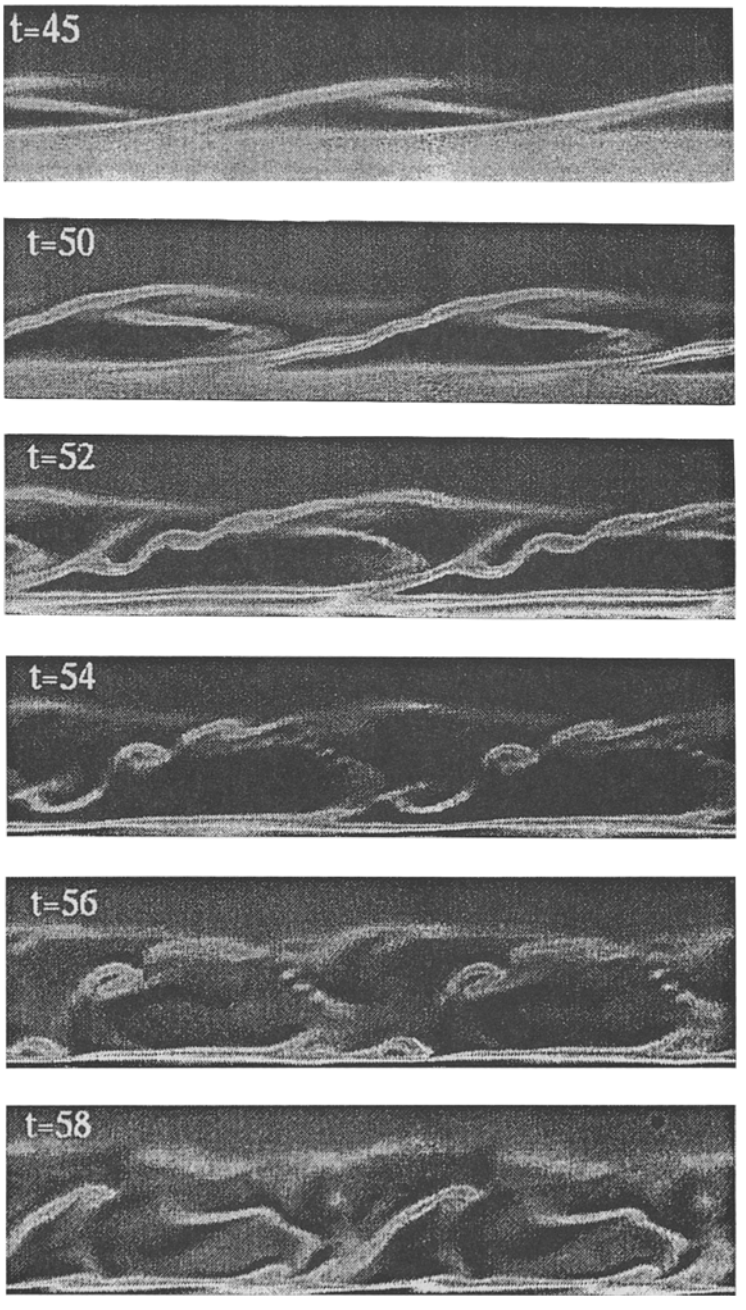

Figure 15. Structure of the spanwise vorticity of the flow field in the transition region with LES and contraction c_1.

structure of the flow field during the entire transition region and for the beginning of the turbulent region. The figure shows different stages: the formation of the lambda vortices, the development of the high-shear layers, the appearance of spikes, the decay of the large-scale structure, and the formation of new, small structures.

Structure Function Dynamic Model

When the grid 48 × 24 × 96 is used in LES, we notice that the formulation with contraction c_2 is less successful than the formulation with contraction c_1 in predicting the correct energy content (compared with fine-grid DNS) of various Fourier modes; contraction c_2 seems more dissipative late in the transition region. This is also demonstrated in Figure 13 and 14, where, in the middle of the transition region, differences appear in the structure of the vorticity field for contraction C_2. We know that contraction c_2 produces model coefficients that are different from the other contraction (C_r and C_θ are lower, and C_i is higher as shown in Figure 4). The direct influence of that on the modeled values of the local SGS field can hardly explain the reason for these differences. The energy balance and interaction between the large and SGS fields during the simulation produce different levels of eddy viscosity and eddy diffusivity for each contraction. In their LES of incompressible scaler transport with the dynamic model ($C_i = 0$), Cabot and Moin [37] tested both contractions and found that the least-squares contraction (contraction c_2) is the least SGS dissipative and its results matches better with DNS; a conclusion that is opposite to ours. This suggests that our LES results are sensitive to the model coefficient C_i, and the energy balance between the large and subgrid scales is also sensitive to the contraction type. Because the grid-filter width also controls the energy balance between the large and subgrid scales, we conclude that the grid-filter width which we chose for LES formulation with contraction c_1 is not suitable for LES formulation with contraction c_2. The way to go about increasing or decreasing the filter width for contraction c_2 to match the solution of contraction c_1 cannot be simply inferred. Instead of repeating the LES calculations with contraction C_2 on another grid, we use the same grid 48 × 24 × 96 with a new proposed dynamic model.

All dynamic-modeling investigators have used the Smagorinsky eddy-viscosity closure to model the SGS stresses (as introduced in the previous section) thereby inheriting some of the limitations mentioned before about the Smagorinsky model and losing some of the advantages of the dynamic procedure. Recently, El-Hady [38] has proposed a dynamic SGS model that utilizes the second-order velocity structure function to parametrize the small-scale field. The structure function by itself is known to furnish better results than the Smagorinsky model, particularly in highly intermittent regions [15], [17]. The new model appears to have the potential to predict the details of the transitional flow field better than the Smagorinsky-based dynamic model.

Analogous to (29) and (30), we model the eddy viscosity ν_t, the eddy diffusivity α_t, and the SGS kinetic energy K_s as

$$\nu_t(\mathbf{x}, t) = C_r \bar{\rho} \Delta [\tilde{F}_2(\mathbf{x}, \Delta, t)]^{1/2}, \tag{53}$$

$$\alpha_t(\mathbf{x}, t) = C_\theta \bar{\rho} \Delta [\tilde{F}_2(\mathbf{x}, \Delta, t)]^{1/2}, \tag{54}$$

$$K_s = 2 C_i \bar{\rho} \Delta [\tilde{F}_2(\mathbf{x}, \Delta, t)]. \tag{55}$$

Here, we follow Normand and Lesieur [24] and use the following four-point expression for the structure function $\tilde{F}_2(\mathbf{x}, \Delta, t)$ because of the flow homogeneity in the two periodic directions:

$$\tilde{F}_2 = \tfrac{1}{4}\left[\left(\frac{\Delta}{\Delta x}\right)^2 (\|\mathbf{v}(x + \Delta x, y, z, t) - \mathbf{v}(x, y, z, t)\|^2 + \|\mathbf{v}(x, y, z, t) - \mathbf{v}(x - \Delta x, y, z, t)\|^2) + \left(\frac{\Delta}{\Delta z}\right)^2 (\|\mathbf{v}(x, y, z + \Delta z, t) - \mathbf{v}(x, y, z, t)\|^2 + \|\mathbf{v}(x, y, z, t) - \mathbf{v}(x, y, z - \Delta z, t)\|^2)\right], \tag{56}$$

and the characteristic grid-filter width is $\Delta = \min(\Delta x, \Delta z)$. Here, we generalize the structure-function model [15] to include compressibility effects and energy transport.

We follow the procedure of dynamic modeling, and apply a test filter of larger width $\hat{\Delta}$ to the resolved field. We use a sharp Fourier cutoff filter in the two homogeneous directions x and z and keep the ratio $\eta = 2$. If we assume the same functional form and model coefficients, then the "test" eddy coefficients and "test" SGS kinetic energy are modeled the same way as the "grid" counter-

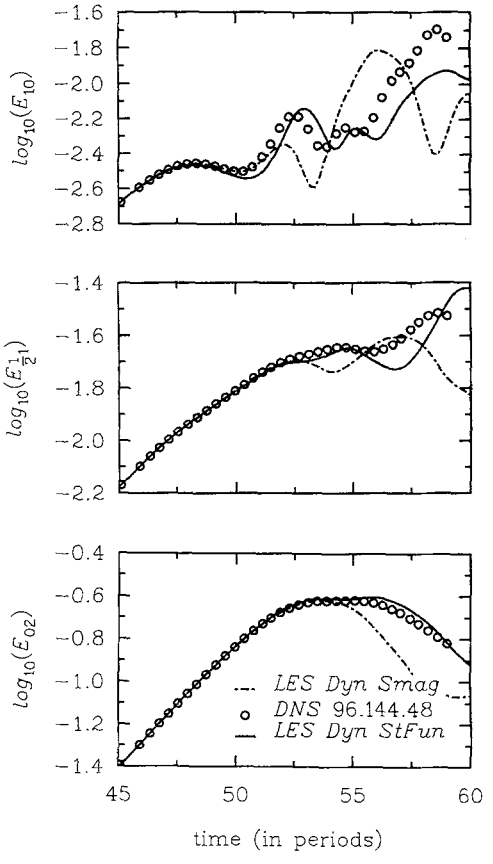

Figure 16. Comparison of the time evolution of the energy content of dominant Fourier harmonics (1, 0), ($\frac{1}{2}$, 1), (0, 2) inside the transition region between the structure-function dynamic model, Smagorinsky-based dynamic model, and fine-grid DNS [29].

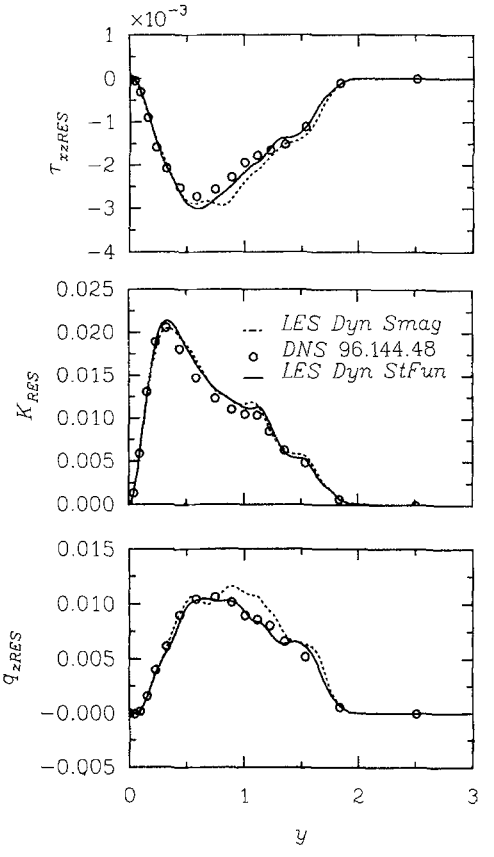

Figure 17. Comparison of resolved Reynolds stress components τ_{xz}, resolved turbulent kinetic energy K, and resolved heat-flux component q_z at $t = 54$ inside the transition region between the structure-function dynamic model, Smagorinsky-based dynamic model, and fine-grid DNS [29].

parts as

$$\hat{\nu}_t(\mathbf{x}, t) = C_r \hat{\bar{\rho}} \hat{\Delta} [\hat{\bar{F}}_2(\mathbf{x}, \hat{\Delta}, t)]^{1/2}, \tag{57}$$

$$\hat{\alpha}_t(\mathbf{x}, t) = C_\theta \hat{\bar{\rho}} \hat{\Delta} [\hat{\bar{F}}_2(\mathbf{x}, \hat{\Delta}, t)]^{1/2}, \tag{58}$$

$$\hat{K}_s = 2C_i \hat{\bar{\rho}} \hat{\Delta} [\hat{\bar{F}}_2(\mathbf{x}, \hat{\Delta}, t)]. \tag{59}$$

Then we follow the dynamic procedure as detailed before to determine the model coefficients C_r, C_i, and C_θ.

Figure 16 shows a close comparison of the evolution of the energy content of the dominant modes inside the transition region between the LES with the structure-function dynamic model, the LES with the Smagorinsky-based dynamic model (both have identical grid histories, and use contraction c_2), and the fine-grid DNS [29]. Results with the structure-function dynamic model are in good agreement with the DNS and the model is capable of predicting the correct energy content of various Fourier modes throughout the transition region (notice the excellent prediction of the energy content of mode (0, 2), which dominates the transition region); in the case of the dynamic eddy-viscosity model, the comparison is poor shortly after the onset of transition. Figure 17 compares some of the resolved components of the Reynolds stresses and heat flux as well as the resolved turbulent kinetic energy inside the transition region (at $t = 54$). Compared with the DNS results, the structure-function dynamic model predicts these quantities better than the Smagorinsky-based dynamic model. Figure 18 shows the excellent prediction of the flow structure in terms of the spanwise vorticity when using the structure-function dynamic model.

DNS 96 × 144 × 48

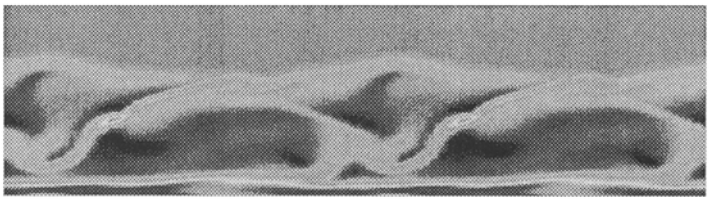

LES 36 × 96 × 24 Structure Function Dynamic Model

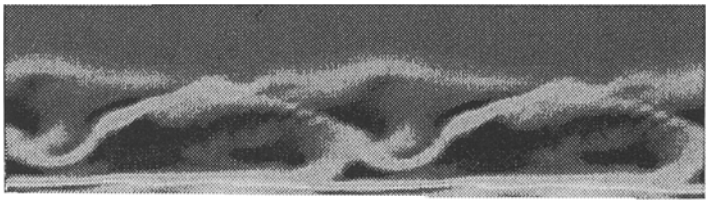

LES with Smagorinsky-Based Dynamic Model

Figure 18. Comparison of the spanwise component of vorticity at $t = 54$ between the structure-function dynamic model, Smagorinsky-based dynamic model, and fine-grid DNS [29].

5. Concluding Remarks

The nonlinear evolution and breakdown of the laminar boundary layer in high-speed flows is investigated with LES. The dynamic eddy-viscosity SGS models of Germano *et al.* [19] and Moin *et al.* [27] have been applied to determine dynamically the model coefficients. The model gives the proper asymptotic behavior near the wall and vanishes in the free stream without the need for *ad hoc* damping functions. The values of the model coefficients are almost negligible in the linear and early nonlinear stages and increase sharply in the wall region as the breakdown progresses. As the turbulent stage approaches, the values of the model coefficients drop and are not confined to the wall region, but spread away from the wall.

The model has no dissipative character like the standard Smagorinsky model. The LES with the dynamic model is able to capture the periodic lambda-shaped vortices and the "rope-like" wave structure at the early stages even with the coarse grid 24 × 96 × 12.

The LES with the dynamic model is able to capture the bulk of the flow-field structure inside the transition region. While both contractions give identical results at the early stages of the transition, slight differences in the details of the flow structure occur in the late stages of transition. For these stages, the LES flow-field structure with contraction c_1 compares more favorably with the DNS results. When the structure-function dynamic model of El-Hady [38] is used with contraction C_2, the results compare favorably with the DNS results.

Large-eddy simulation of transitional flow along a cylinder at Mach 4.5 is achieved with one-sixth of the grid resolution that was used for DNS. The structure of the flow field during the entire transition region and the beginning of the turbulent region is demonstrated with LES.

One final note about the nature of the simulation in this study. The temporal simulation offers, qualitatively, a more economic way to help understand the physics of transition. However, the spatial evolution of disturbances and a meaningful transition prediction can only be described (accurately) by spatial simulations. The successful application of LES with dynamic modeling to compute through the

transitional regime of a high-speed flow in a temporal simulation, promises a successful extension to a true spatially evolving boundary layer; this work is in progress.

Acknowledgements

The authors acknowledge the valuable discussions with Dr. David Pruett of Analytical Services and Materials, Inc., and Prof. Ugo Piomelli of the University of Maryland, the constructive comments made by the referees, and the support of NAS computational resources.

References

[1] Mack, L.M. Review of linear compressible stability theory. In *Stability for Time Dependent and Spatially Varying Flows*, D.L. Dwoyer and M.Y. Hussaini, eds. Springer-Verlag, New York, 1985, pp. 164–187.

[2] El-Hady, N.M. Secondary instability of high-speed flows and the influence of wall cooling and suction. *Phys. Fluids A*, vol. 4, no. 4, 1992, pp. 727–743.

[3] Pruett, D.C., Ng, L.L., and Erlebacher, G. On the nonlinear stability of a high-speed, axisymmetric boundary layer. *Phys. Fluids A*, vol. 3, no. 12, 1991, pp. 2910–2926.

[4] Kendall, J.M., Jr. Wind tunnel experiments relating to supersonic and hypersonic boundary-layer transition. *AIAA J.*, vol. 13, 1975, pp. 290–299.

[5] Stetson, K.F., and Kimmel, R.L. On the Breakdown of a Hypersonic Laminar Boundary Layer. AIAA Paper No. 93-0896, 1993.

[6] Bertolotti, F.P., and Herbert, T. Analysis of the linear stability of compressible boundary layers using the PSE. *Theoret. Comput. Fluid Dynamics*, vol. 3, 1991, 177–124.

[7] Chang, C.-L., Malik, M.R., Erlebacher, G., and Hussaini, M.Y. Compressible Stability of Growing Boundary Layers Using Parabolized Stability Equations. AIAA Paper No. 91-1636, 1991.

[8] Singer, B.A. Modeling of the Transition Region. NASA CR 4492, February 1993.

[9] Smagorinsky, J. General circulation experiments with the primitive equations. I. The basic experiment. *Monthly Weather Rev.*, vol. 91, 1963, pp. 99–164.

[10] Moin, P., and Kim, J. Numerical investigation of turbulent channel flow. *J. Fluid Mech.*, vol. 118, 1982, pp. 381–392.

[11] Piomelli, U., and Zang, T.A. Large-eddy simulation of transitional channel flow. *Comput. Phys Comm.*, vol. 65, 1991, pp. 224–230.

[12] Piomelli, U., Zang, T.A., Speziale, C.G., and Hussiani, M.Y. On the large eddy simulation of transitional wall-bounded flows. *Phys. Fluids A*, vol. 2, no. 2, 1990.

[13] Kraichnan, R.H. Eddy viscosity in two and three dimensions. *J. Atmospheric Sci.*, vol. 33, 1976, pp. 1521–1536.

[14] Chollet, J.P., and Lesieur, M. Parameterization of small scales of three-dimensional isotropic turbulence utilizing spectral closures. *J. Atmospheric Sci.*, vol. 38, 1981, pp. 2747–2757.

[15] Metais, O., and Lesieur, M. Spectral large-eddy simulation of isotropic and stably stratified turbulence. *J. Fluid Mech.*, vol. 239, 1992, pp. 157–194.

[16] Comte, P., Lee, S., and Cabot, W.H. A subgrid-scale model based on the second order velocity structure function. *CTR Proceedings of the Summer Program*, Stanford University, 1990, pp. 31–45.

[17] Silveira, N.A., Grand, D., Metais, O., and Lesieur, M. Large-eddy simulation of the turbulent flow in the downstream region of a backward-facing step. *Phys. Rev. Lett.*, vol. 66, 1991, pp. 2320–2323.

[18] Germano, M. Turbulence: the filtering approach. *J. Fluid Mech.*, vol. 238, 1992, pp. 325–336.

[19] Germano, M., Piomelli, U., Moin, P., and Cabot, W. A dynamic subgrid-scale eddy viscosity model. *Phys. Fluids A*, vol. 3, no. 7, 1991, pp. 1760–1765.

[20] Speziale, C.G., Erlebacher, G., Zang, T.A., and Hussiani, M.Y. The subgrid-scale modeling of compressible turbulence. *Phys. Fluids*, vol. 31, no. 4, 1988, pp. 940–942.

[21] Erlebacher, G., Hussiani, M.Y., Speziale, C.G., and Zang, T.A. Toward the large-eddy simulation of compressible turbulent flows. *J. Fluid Mech.*, vol. 238, 1992, pp. 155–185.

[22] Bardina, J., Ferziger, J.H., and Reynolds, W.C. Improved Subgrid-Scale Models for Large-Eddy Simulation. AIAA Paper No. 80-1357, 1980.

[23] Zang, T.A., Dahlburg, R.B., and Dahlburg, J.P. Direct and large-eddy simulations of three-dimensional compressible Navier–Stokes turbulence. *Phys. Fluids A*, vol. 4, no. 1, 1992, pp. 127–140.

[24] Normand, X., and Lesieur, M. Direct and large-eddy simulations of transition in the compressible boundary layer. *Theoret. Comput. Fluid Dynamics*, vol. 3, 1992, pp. 231–252.

[25] Kral, L.D., and Zang, T.A. Large-eddy simulation of supersonic, wall-bounded turbulent flows. In *Transition and Turbulence*, Proc. ICASE/NASA Workshop, Springer-Verlag, 1992.

[26] Zang, T.A., Chang, C-L., and Ng, L.L. The transition prediction toolkit: LST, SIT, PSE, DNS and LES, *Proc. Fifth Symposium on Numerical and Physical Aspects of Aerodynamic Flows*, Long Beach, CA, January 13–15, 1992.

[27] Moin, P., Squires, K., Cabot, W., and Lee, S. A dynamic subgrid-scale model for compressible turbulence and scalar transport. *Phys. Fluids A*, vol. 3, no. 11, 1991, pp. 2746–2757.

[28] El-Hady, N.M., Zang, T.A., and Piomelli, U. Dynamic subgrid-scale modeling for high-speed transitional boundary layers. In *Proc. Symposium on Engineering Applications of Large-Eddy Simulations*, 1993 Fluids Engineering Conference, Washington, D.C., June 20–23, 1993.

[29] Pruett, C.D., and Zang, T.A. Direct numerical simulation of laminar breakdown in high-speed, axisymmetric boundary layers. *Theoret. Fluid Dynamics*, vol. 3, no. 6, 1992, pp. 345–367.

[30] Piomelli, U., Moin, P., and Ferziger, J.H. Model consistency in large eddy simulation of turbulent channel flows. *Phys. Fluids*, vol. 31, no. 7, 1988, pp. 1884–1891.

[31] Gosal, S., and Moin, P. The basic equations for the LES of turbulent flows in complex geometry. *Bull. Amer. Phys. Soc.*, vol. 38, no. 12, 1993, p. 2189.

[32] Lilly, D.K. A proposed modification of the Germano subgrid scale closure method. *Phys. Fluids A*, vol. 4, no. 3, 1992, pp. 633–635.

[33] Piomelli, U., Cabot, W.H., Moin, P., and Lee, S. Subgrid-scale backscatter in turbulent and transitional flows. *Phys. Fluids A*, vol. 3, no. 7, 1991, pp. 1766–1771.

[34] Erlebacher, G., and Hussaini, M.Y. Numerical experiments in supersonic boundary-layer stability. *Phys. Fluids A*, vol. 2, no. 1, 1990, pp. 94–104.

[35] Pruett, C.D., and Streett, C.L. A spectral collocation method for compressible, nonsimilar boundary layers. *Internat. J. Numer. Methods Fluids*, vol. 13, no. 6, 1991, pp. 713–737.

[36] El-Hady, N.M., Zang, T.A., and Piomelli, U. Application of the dynamic subgrid-scale model to axisymmetric transitional boundary layer at high speed. *Phys. Fluids*, vol. 6, no. 3, 1994, pp. 1299–1309.

[37] Cabot, W., and Moin, P. Large eddy simulation of scalar transport with the dynamic subgrid-scale model. In *Large Eddy Simulation of Complex Engineering and Geophysical Flows*, B. Galperin and S. Orszag, eds., Cambridge University Press, Cambridge, 1993.

[38] El-Hady, N.M. Structure function dynamic subgrid-scale model. In *Transition, Turbulence, and Combustion*, M. Hussaini, T. Jackson, and T. Gatski, eds., Springer-Verlag, New York, 1994. Also in *Bull. Amer. Phys. Soc.*, vol. 38, no. 12, p. 2190.